Indentation of a Free-Falling Sharp Penetrometer into a Poroelastic Seabed

Dae Sung Lee[1] and Derek Elsworth[2]

Abstract: A solution is developed for the buildup, steady, and postarrest dissipative pore fluid pressure fields that develop around a conical penetrometer that self-embeds from free-fall into the seabed. Arrest from free-fall considers deceleration under undrained conditions in a purely cohesive soil, with constant shear strength with depth. The resulting decelerating velocity field is controlled by soil strength, bearing capacity factors, and inertial components. At low impact velocities the embedment process is controlled by soil strength, and at high velocities by inertia. With the deceleration defined, the solution for a point normal dislocation migrating in a poroelastic medium is extended to incorporate the influence of a tapered tip. Dynamic steady pressures, P_D, develop relative to the penetrating tip geometry with their distribution conditioned by the nondimensional penetration rate, U_D, incorporating impacting penetration rate, consolidation coefficient, and penetrometer radius, and the nondimensional strength, N_D, additionally incorporating undrained shear strength of the sediment. Pore pressures may develop to a steady peak magnitude at the penetrometer tip, and drop as $P_D = 1/x_D$ with distance x_D behind the tip and along the shaft. Induced pore pressures are singular in the zone of tip taper for the assumed zero radius of the penetrometer, negating the direct evaluation of permeability magnitudes from pressures recorded on the cone face. However, peak induced pressure magnitudes may be correlated with sediment permeabilities, postarrest dissipation rates may be correlated with consolidation coefficients, and depths of penetration may be correlated with shear strengths. The magnitudes of fluid pressures evaluated on the shaft may be correlated with sharp penetrometer data (reported by Urgeles et al. in 2000) to independently evaluate magnitudes of strength and transport parameters.

DOI: 10.1061/(ASCE)0733-9399(2004)130:2(170)

CE Database subject headings: Permeability; Pore pressure; Penetrometers; Poroelasticity; Marine clays.

Introduction

Tethered and untethered penetrometers are widely used for the determination of seabed (Richards et al. 1975, for example) and lakebed (Lee 1977; Harvey et al. 1997, for example) characteristics. Of prime interest here is the determination of fluid, mass (chemical), and thermal fluxes on continental margins and in abyssal sediments (Schultheiss and Noel 1986, for example), with ancillary interest in strength parameters that define stability against submarine slope failure (Watts and Masson 1995, for example). Mass, chemical, and thermal fluxes may be evaluated from differential fluid pressures, species concentrations, or temperatures with depth along the embedded lance axis; these data must be combined with Darcy's, Fick's, or Fourier's laws, respectively. Implicit in the evaluation is that permeability of the sediments may be independently defined to enable fluid mass flux to be accurately determined, with potential coupling to advective components of chemical or thermal fluxes.

[1]Dept. of Energy and Geo-Environmental Engineering, Pennsylvania State Univ., University Park, PA 16802-5000.

[2]Dept. of Energy and Geo-Environmental Engineering, Pennsylvania State Univ., University Park, PA 16802-5000.

Note. Associate Editor: Victor N. Kaliakin. Discussion open until July 1, 2004. Separate discussions must be submitted for individual papers. To extend the closing date by one month, a written request must be filed with the ASCE Managing Editor. The manuscript for this paper was submitted for review and possible publication on May 10, 2002; approved on June 12, 2003. This paper is part of the ***Journal of Engineering Mechanics***, Vol. 130, No. 2, February 1, 2004. ©ASCE, ISSN 0733-9399/2004/2-170–179/$18.00.

Current methods of determining the permeability of the penetrated sediments involve first evaluating hydraulic diffusivity from the dissipation rate of the penetration-induced pore fluid pressures (Torstensson 1977; Robertson et al. 1986; Levadoux and Baligh 1986; Baligh and Levadoux 1986; Robertson et al. 1992). This requires that the strain field around the penetrometer be defined by analytical (Ladanyi 1963; Vesic 1972; Baligh and Scott 1976; Drescher and Kang 1987) or numerical (Baligh 1985; Tumay et al. 1985; Acar and Tumay 1986) methods, and pore pressures estimated by coupling with an appropriate constitutive model (Skempton 1954; Biot and Willis 1957). Permeability is subsequently determined from hydraulic diffusivity through knowledge of the drained deformation modulus, E, or reciprocally analogous coefficient of volume compressibility, m_v, or ''frame'' compressibility (Levadoux and Baligh 1986; Robertson et al. 1992). The drained modulus is determined either from laboratory testing of recovered sediment samples, or in some cases from the reduction of tidally induced pore fluid pressures (Davis et al. 1991; Fang et al. 1993; Wang and Davis 1996). Of these two methods, the latter is most desirable, since in situ response is recorded for a relatively large representative sediment volume. However, depending on fixed tidal frequency and the relative moduli and permeabilities of the sediment, phase offsets and pressure amplitude profiles with depth may be difficult to resolve for the determination of permeabilities (Wang and Davis 1996). This is especially true where permeabilities are relatively high, and the phase offset is essentially absent. Alternatively, the use of maximum pore pressure magnitudes developed during penetrometer insertion provides a one-step method to determine permeability magnitudes (Elsworth 1993, 1998). This procedure offers the po-

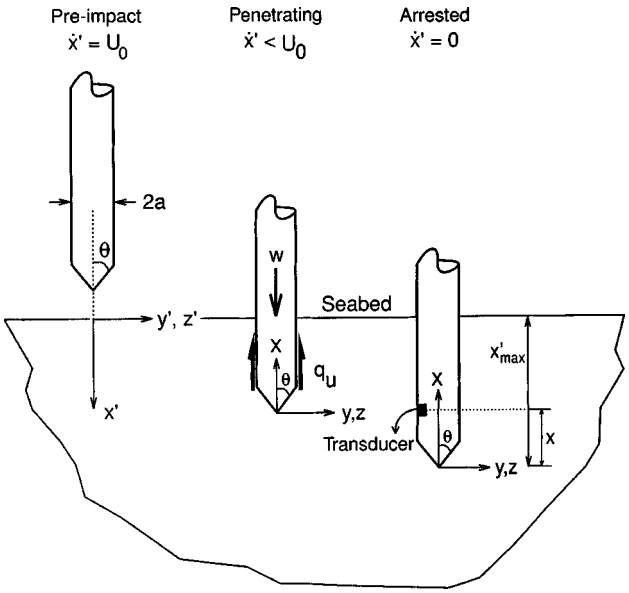

Fig. 1. Schematic of a lance falling at terminal velocity, U_0, and impacting the seabed. For embedment, the coordinate system is fixed to the seafloor as the lance self-embeds under undrained conditions. For the evolving partially drained analysis of embedment-generated pore pressures, the coordinate system is fixed to the penetrometer tip.

tential to provide independent corroboration of permeabilities where they are determined by other means, and permeability magnitudes where they are otherwise unavailable.

Many of the difficulties involved in determining permeability using current techniques may be resolved if the magnitude of penetration-induced pore pressure is used as an index to define permeability. From this approach, permeability magnitudes are available directly from the combined early time pressure data, and lance deceleration response. Hydraulic diffusivities, c, are available from the dissipation response, enabling frame compressibility, and potentially undrained sediment strength, to be recovered, without recourse to additional laboratory testing. The utility of this approach is examined in the following.

The following analysis addresses this complex problem by, for the first time, evaluating penetration induced pore pressures around a decelerating tapered probe. This is evaluated in two steps; first the rate of deceleration of the lance as it impacts the soft seabed is determined, and then used to evaluate the resulting pore pressure distributions that develop around the embedding tip and shaft.

This analysis may be extended to include the local geometry of the penetrometer tip by using a distribution of volumetric dislocations that closely approximate the geometry of tip advance. This is completed in the following.

Embedment Deceleration

Consider a sharp lance falling through the water column that has reached terminal velocity, U_0, and subsequently impacts the soft sediments of the seabed, as illustrated in Fig. 1. These soft sediments are assumed cohesive only, and in the time frame of deceleration of the lance, behave as undrained, for the purposes of this first evaluation. The undrained cohesive strength, S_u, is constant with depth, and the lance is sufficiently long that the tip-region is short in comparison with the overall length of the penetrometer. Where strength is linearly varying, an average strength magnitude representative of the depth profile may be substituted. As the lance tip, assumed sharp in this analysis, embeds within the soil to a distance x' below the seabed surface, the force resisting embedment builds. The bearing capacity, q_u, of the lance may be defined in terms of the end-bearing area, A_p, and shaft area, A_s, as

$$q_u = A_p(S_u N_c + \sigma_{vo}) + A_s S_u \tag{1}$$

where σ_{vo} = total stress, absent the sea pressure, at current tip embedment-depth, x'; and N_c = nondimensional bearing capacity factor, typically approaching 9 for depth to diameter ratios greater than 4.5 (Skempton 1959). The rightmost two terms of stress and shaft friction vary linearly with embedment depth, x', and Eq. (1) may be redefined as

$$q_u = A_p S_u N_c + (A_p \gamma_s + 2\pi a S_u)x' \tag{2}$$

where the probe diameter is $2a$, and γ_s = drained unit weight of the soil. The penetrometer is assumed blunt in order to render the analysis of undrained penetration tractable. Alternatively, the bearing force, acting in the direction of negative x', may be defined as a linear function of depth as

$$q_u = N'_c + N'_q x' \tag{3}$$

This enables a force balance to be completed on the free-falling penetrometer as it embeds in the seabed, and the end-bearing force builds approximately linearly with embedment. Balancing the vertically downward absolute mass, w, and buoyant mass, w_b, of the penetrometer with the vertically upward resistance, q_u, of the combined end- and shaft-resistance, yields, when balanced with inertial force

$$w\ddot{x}'[t] = w_b g - N'_c - N'_q x'[t] \tag{4}$$

The double overdot represents acceleration. The lance is rigid, and translates with the motion of the tip, indexed in this relation as x'. The initial conditions are set at time $t=0$ when the lance-tip first impacts the seabed at velocity, U_0, as

$$x'[t=0] = 0$$
$$\dot{x}'[t=0] = U_0 \tag{5}$$

Solving the differential equation (4) for the boundary conditions of Eq. (5) enables the progress of embedment with time to be defined as

$$x'[t] = \frac{(gw_b - N'_c)}{N'_q}\left[1 - \cos\left(\sqrt{\frac{N'_q}{w}}t\right)\right] + U_0\sqrt{\frac{w}{N'_q}}\sin\left(\sqrt{\frac{N'_q}{w}}t\right) \tag{6}$$

and for the change in velocity, $\dot{x}'[t]$, with time as

$$\dot{x}'[t] = \frac{(gw_b - N'_c)}{N'_q}\sqrt{\frac{N'_q}{w}}\sin\left(\sqrt{\frac{N'_q}{w}}t\right) + U_0\cos\left(\sqrt{\frac{N'_q}{w}}t\right) \tag{7}$$

In the solutions for both embedment length and velocity, the two terms represent, respectively, noninertial penetration under self-weight (first term), and the inertial component of the lance (second term). Solving for the time until arrest is possible by setting Eq. (7) to zero as $\dot{x}'[t]=0$ when deceleration is complete. This yields

$$t|_{\dot{x}'=0} = \sqrt{\frac{w}{N'_q}}\arctan\left(-\frac{U_0 N'_q}{(gw_b - N'_c)}\sqrt{\frac{w}{N'_q}}\right) \tag{8}$$

for the time to arrest, or alternatively the embedment length $x'_{\max}$, as

$$x'_{\max}=\left(\frac{gw_b-N'_c}{N'_q}\right)+\left[\left(\frac{gw_b-N'_c}{N'_q}\right)^2\cdot\frac{N'_q}{w}\frac{1}{U_0}+U_0\sqrt{\frac{w}{N'_q}}\right]\times\sin\left(\sqrt{\frac{N'_q}{w}}t\bigg|_{\dot{x}'=0}\right) \tag{9}$$

This complex relation may be simplified by realizing there are two regimes of penetration; that where inertial effects are negligible, for small U_0, and alternatively where inertial effects dominate. From Eq. (7), at slow penetration velocities, as $U_0\rightarrow 0$ then

$$U_0\ll\frac{(gw_b-N'_c)}{N'_q}\sqrt{\frac{N'_q}{w}} \tag{10}$$

and $t\sqrt{N'_q/w}=0$. Substituting this into Eq. (6) yields a trivial solution of zero embedment as $x'|_{\max}=0$. This condition is met when $N'_c\gg N'_q$, and surface bearing capacity greatly exceeds the influence of bearing at depth. The corollary to the noninertial condition is where the impact velocity is comparatively large. For this condition

$$U_0\gg\frac{(gw_b-N'_c)}{N'_q}\sqrt{\frac{N'_q}{w}}\quad\text{then from Eq. (7)}\quad\sqrt{\frac{N'_q}{w}}t=\frac{\pi}{2} \tag{11}$$

Substituting Eq. (11) into Eq. (6) results in a maximum embedment depth, $x'|_{\max}$, of

$$x'|_{\max}=U_0\sqrt{\frac{w}{N'_q}} \tag{12}$$

occurring at time

$$t=\frac{\pi}{2}\sqrt{\frac{w}{N'_q}} \tag{13}$$

The consequence of Eq. (12) is that shear strength, S_u, may be determined from either knowledge of the impact velocity and embedment length, or from knowledge of the time to decelerate to zero velocity. Each reduction method enables N'_q to be determined, and hence S_u, if lance geometry and weight are known. An alternative to using a point measurement of time-to-arrest or embedment-length is to fit the recorded velocity history to the rearranged Eq. (7) as

$$N'_q=\left[\arccos\left(\frac{\dot{x}'[t]}{U_0}\right)\frac{\sqrt{w}}{t}\right]^2 \tag{14}$$

This enables N'_q and hence S_u to be recovered from the deceleration history. Where the impact velocity, U_0, is significant, as $U_0\gg(gw_b-N'_c)/n'_q\sqrt{N'_q/w}$, then the embedment history simplifies to

$$\dot{x}'[t]=U_0\cos\left(\sqrt{\frac{N'_q}{w}}t\right)=U \tag{15}$$

for velocity, and

$$x'[t]=U_0\sqrt{\frac{w}{N'_q}}\sin\left(\sqrt{\frac{N'_q}{w}}t\right) \tag{16}$$

for embedment depth. These relations may be used to evaluate the development of pore fluid pressures that result from penetration, where the requirement for undrained penetration is relaxed. Pore pressures generated around the decelerating probe may be determined from the approximate probe velocity as the unit decelerates.

Dislocation Analysis

The behavior of a sharp penetrometer, moving within a poroelastic medium, may be represented by a moving volumetric dislocation. The incremental form of this is a point volumetric dislocation, of volume dV (L^3), representing the dilation in unit time, t, subjected to a volumetric dilation rate, v (L^3T^{-1}), as $dV=v\,dt$. For $t\geq 0$ a volumetric dislocation is introduced at the origin ($x=y=z=0$) with the poroelastic medium moving at velocity $+U$ in the x-direction of the fixed Cartesian coordinate system, representing a dislocation migrating within an infinite medium, as illustrated in Fig. 1. The velocity of migration is $U=U_0\cos(bt)$, and the location at time, t, is $x'[t]=(U_0/b)\sin(bt)$, where $b=\sqrt{N'_q/w}$ as identified in Eqs. (2), (3), and (4). The position of a point located at (x,y,z) at time t would have been $(\{x-(U_0/b)\sin[b(t-\tau)]\},y,z)$ at time τ. This migrating coordinate system enables the behavior to be defined for a static dislocation (Cleary 1977; Elsworth 1991)

$$p-p_s=\frac{c\,dV}{4\pi\tilde{R}^3}\frac{\mu}{k}\frac{\tilde{\xi}^3}{2\sqrt{\pi}}e^{-\tilde{\xi}^2/4} \tag{17}$$

with $\tilde{\xi}=\tilde{R}/\sqrt{c(t-\tau)}$ and $\tilde{R}^2=\{x-(U_0/b)\sin[b(t-\tau)]\}^2+y^2+z^2$. The material properties defining the medium represent absolute pore fluid pressure, p, relative to the initial static fluid pressure, p_s, permeability, k, hydraulic diffusivity, c, and dynamic viscosity of the fluid, μ. Although derived for an orthogonal triplicate of force dipoles, representing the volumetric dilation of a cube in a poroelastic medium (Cleary 1977), the undefined volume dilation may be indexed to the compressibility of the surrounding medium (Elsworth 1991; 1992). Physically, a migrating dislocation represents a volume of fluid equivalent to the volume of the soil and water mixture displaced by the injection of the penetrometer. It is feasible to represent the pressures induced by the instantaneous injection of a volume of fluid, dV. Substituting into Eq. (17) for the incremental rate of dilation as $dV=v\,d\tau$, and integrating in time yields

$$p-p_s=\int_0^t\frac{cv}{4\pi\bar{R}^3}\frac{\mu}{k}\frac{\bar{\xi}^3}{2\sqrt{\pi}}e^{-\bar{\xi}^2/4}d\tau \tag{18}$$

where v is the rate of volume change (L^3T^{-1}).

This is similar to the standard result reported (Elsworth 1991) for a penetrometer moving at constant velocity, v. To determine the form of the fluid pressure field that develops around a decelerating penetrometer, tapered along its axis, the response for a point volumetric dislocation must be distributed to represent the moving feature. Consider the conical tip of a penetrometer of radius, a, as illustrated in Fig. 2, where the semiapical angle, θ, and length of taper, l, define the geometry. A surrogate variable χ is selected that parallels the x axis that may be used for integrating an appropriately weighted distribution of the point dislocations. Correspondingly, the projected area, dA, of a circumferential contour on the y-, z-plane is defined

$$dA=2\pi r'dr'\begin{cases}r'=\chi\tan\theta\\ dr'=d\chi\tan\theta\end{cases} \tag{19}$$

which upon substitution of the components of Eq. (19) gives

$$dA=2\pi\tan^2\theta\,\chi\,d\chi \tag{20}$$

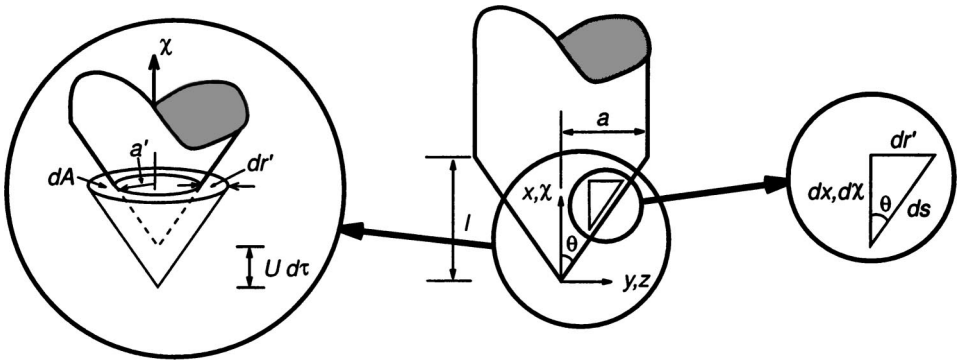

Fig. 2. Geometry of cone tip (center) defininining length of taper, l, semiapical angle, θ, and shaft radius, a. Coordinate system is attached to the cone apex and migrates with the penetrometer at velocity, U, in the direction of the negative x or χ axis. Incremental advance of length $Ud\tau$ in time $d\tau$ results in expansion of a cavity (left), defined in magnitude by Eq. (19).

For an incremental advance of the penetrometer of $Ud\tau$ in time $d\tau$, the distribution of volume is $dV=dAUd\tau$, and substituting the relation of Eq. (20), and noting from the previous that $dV=vd\tau$, then

$$v=2\pi\tan^2\theta\chi Ud\chi=2\pi\tan^2\theta\chi U_0\cos[b(t-\tau)]d\chi \quad (21)$$

This may be substituted directly into Eq. (18) to yield

$$p-p_s=\frac{\mu}{k}\frac{\tan^2\theta U_0 c}{4\sqrt{\pi}}\int_0^l\int_0^t\chi\frac{\tilde{\xi}^3}{\tilde{R}^3}e^{-\tilde{\xi}^2/4}\cos[b(t-\tau)]d\tau d\chi \quad (22)$$

where the tilde overbar denotes inclusion of the variable coordinate of integration as $\tilde{x}=x-(U_0/b)\sin[b(t-\tau)]-\chi$ and

$$\tilde{R}=\sqrt{\tilde{x}^2+y^2+z^2} \quad \text{and} \quad \tilde{\xi}=\frac{\tilde{R}}{\sqrt{c(t-\tau)}} \quad (23)$$

representing migrating coordinates and a reciprocal nondimensional time.

Static models are typically restricted to the undrained distributions of pore pressure and their subsequent dissipation, but are also incapable of partial drainage concurrent with penetration. Conversely, the models presented here represent a traveling cavity, not only static conditions. Importantly, it is feasible to represent the dynamic steady pore pressure distribution that evolves around the cone tip (Elsworth 1993), and to readily accommodate partially drained behavior.

The penetrometer decelerates as it enters the half space, although the pore pressure solution is for motion within an infinite medium. This apparent contradiction significantly simplifies the ensuing solution, with little expected loss of applicability or accuracy. Induced pressures, proportional to the tip radius, a, are insignificant beyond 10 radii from the shaft (Levadoux and Baligh 1986; Elsworth 1991) and therefore the influence of the free surface is not felt once insertion has reached beyond this. For the 40 mm diameter probe tip, the 10 radii threshold is passed once the 3 m probe has embedded to 8% of its length. Correspondingly, this simplification will have little adverse effect on the solution.

Nondimensional Parameters

The behavior of the system may be defined in terms of the nondimensional parameters of excess fluid pressure, P_D, penetration rate, U_D, strength, N_D, and time, t_D, as

$$P_D=\frac{4(p-p_s)}{U_0 a}\frac{k}{\mu} \quad (24)$$

$$U_D=\frac{U_0 a}{2c} \quad (25)$$

$$N_D=\frac{ba^2}{2c} \quad (26)$$

$$t_D=\frac{4ct}{a^2} \quad (27)$$

$$(x_D;y_D;z_D)=\frac{1}{a}(x;y;z) \quad (28)$$

with $\tilde{R}_D=\sqrt{\tilde{x}_D^2+y_D^2+z_D^2}$, $\tilde{x}_D=\tilde{x}/a$ or $\tilde{x}_D=x_D-(U_D/N_D)\sin[1/2N_D(t_D-\tau_D)]-\chi_D$. These parameters give, respectively, nondimensional pressures, impact velocities, strength, time, and locations.

These nondimensional parameters may be substituted into Eq. (22) to give, in the final form, the behavior around a tapered penetrometer with tip length, $l_D=l/a$ as

$$P_D=\frac{2\tan^2\theta}{\sqrt{\pi}}\int_0^{l_D}\int_0^{t_D}\chi_D\frac{e^{-\tilde{R}_D^2/(t_D-\tau_D)}}{(t_D-\tau_D)^{3/2}}\times\cos\left[\frac{1}{2}N_D(t_D-\tau_D)\right]d\tau_D d\chi_D \quad (29)$$

This enables magnitudes of pore pressure buildup to be determined following initiation of penetration within an infinite medium. Application to this is described in the following.

Parametric Behavior

Postinitiation Pressure Buildup

The nondimensional pressure, P_D, defined in Eq. (29), may be used to define the buildup of pressure following the impact of the penetrometer with the surface of the seabed. The penetrometer impacts the seabed at velocity U_0, represented in dimensionless magnitude as U_D, and decelerates to arrest. Both the length of embedment at arrest and the time to arrest may be evaluated from Eq. (12). The instant of impact is taken as time $t=0$, when the velocity is U_0, enabling the time to arrest to be defined in non-

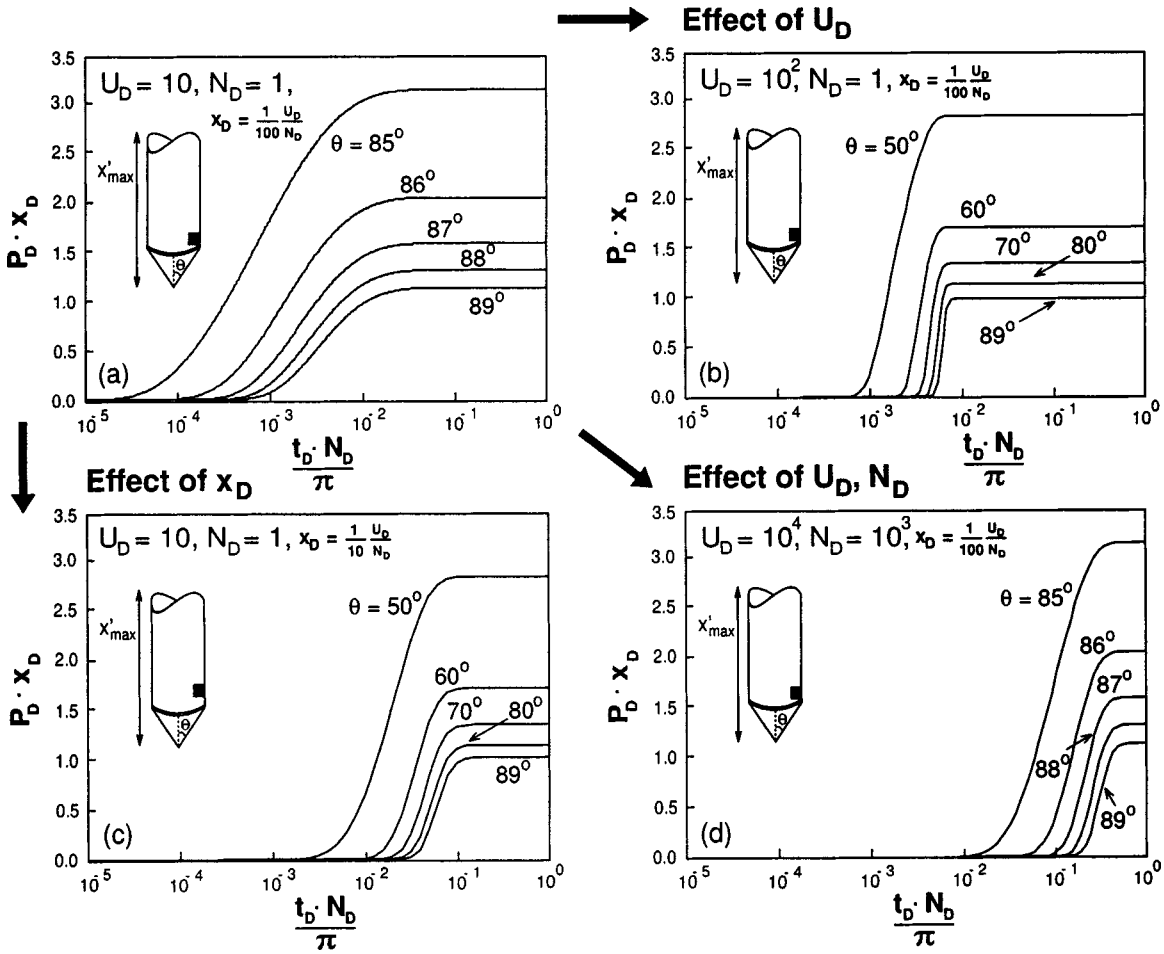

Fig. 3. Buildup of nondimensional pressure, $P_D x_D$, with time, $t_D N_D/\pi$, for a selected pressure monitoring location on the penetrometer shaft, at ordinate (a), (b), and (d) $x_D=(1/100)(U_D/N_D)$, (c) $x_D=(1/10)(U_D/N_D)$, behind the penetrometer tip. This represents a proportional length of 1/100 and 1/10 of the final embedment length behind the penetrometer tip. Pressure response is for various taper angles for the cone, θ, impact velocities, U_D, and material strengths, N_D.

dimensional terms as $t'_D=\pi/N_D$. At this time, the embedment depth is a maximum, with the seabed present to a height of $x'_{D_{max}}=U_D/N_D$ along the shaft.

Pressure buildup response may be evaluated over the period from impact to arrest, for $0<t_D<t'_D$, and for a variety of taper angles for the cone, θ, impact velocities, and material strengths. Impact velocity is represented by U_D, tip length by l_D, and material strength by N_D. For soft seabed clays with undrained strength, S_u, of the order of 10–50 kN/m^2, magnitudes of N_D are in the range 1–1000. It is convenient to compare the buildup of pore pressures with respect to a given location of the transducer at x_D. To make comparisons feasible, we choose the transducer to be above the conical shoulder of the tip, and hence at a location, x_D, greater than the taper lengths, l_D, with respect to the embedment depth, U_D/N_D. This is dependent only on the choice of taper angle for the cone, θ, as $\tan\theta=1/l_D$. Correspondingly, Fig. 3 represents the pressure buildup for the transducer placed one-hundredth $[x_D=(1/100)(U_D/N_D)]$ and one-tenth $[x_D=(1/10)(U_D/N_D)]$ of the distance back from the penetrometer tip, where x is the location of the pressure transducer behind the penetrometer tip. Axes of the figure are selected that take advantage of the known behavior of pressure buildup. Nondimensional pressures are plotted as the product $P_D x_D$, since it is known that the peak pressures shown in this format asymptote to unity as $P_D x_D \rightarrow 1$. Time is reported as $t_D N_D/\pi$, since we know that arrest occurs at $t'_D=\pi/N_D$, hence arrest occurs at $t_D N_D/\pi=1$.

For a sharp penetrometer, the influence of tip taper is prescribed for various taper angles, penetration rates, monitoring locations, and material strengths on the penetrometer shaft. In Fig. 3(a), for monitoring location $x_D=(1/100)(U_D/N_D)$, diffusive response is merely shifted by a one order-of-magnitude increase in taper angles for the cone. Apparent from Fig. 3(a) is that at larger taper angles ($\theta\rightarrow 90°$), the pressure response is close to that of a blunt penetrometer behavior (Elsworth and Lee, unpublished, 2004). In Fig. 3(b), with increased penetration rate, $U_D=10^2$,
and constant monitoring location $[(x_D=(1/100)(U_D/N_D)]$, response time increases, relative to time to arrest as permeability increases. For rapid insertion, the pressure buildup that results from the transducer moving into the pressure bulb is generated essentially instantaneously with insertion and results in the sharp pressure rise apparent in Figs. 3(a and b). As the pressure monitoring location is moved further from the tip to one-tenth $[x_D=(1/10)(U_D/N_D)]$ of the embedment depth from one-hundredth $[x_D=(1/100)(U_D/N_D)]$ of the embedment depth as illustrated in Fig. 3(c), the diffusive response is shifted in time. This represents the time that the transducer enters the sharply defined pressure bulb created by the penetrometer as it

enters the seabed. For the increased material strength, $N_D=10^3$, penetration rate, $U_D=10^4$, and constant monitoring location $[x_D=(1/100)(U_D/N_D)]$ as illustrated in Fig. 3(d), response time increases and the pressure response at larger taper angles ($\theta\rightarrow 90°$) asymptote to unity, as $P_D x_D\rightarrow 1$.

Peak Pressure Magnitudes

Unlike penetration at constant velocity, U, where the pressures build to a dynamic steady state (Elsworth 1991), the peak pressures of interest for the decelerating penetrometer occur at the time of penetrometer arrest. From this state the pressures then dissipate. The distribution of peak pressures on the shaft of a decelerating penetrometer may be determined from $t|_{\dot{x}'=0}$, defined in Eq. (8), and resubsitituted into Eq. (29), as $t'_D=\pi/N_D$. Since the penetrometer may arrest before it reaches a steady pressure distribution, it is likely that the pressure induced around a decelerating penetrometer may, in some circumstances, be less than for steady penetration.

This is the steady solution where the pore fluid pressure remains constant around the tip of the penetrometer when viewed relative to migrating coordinate system. Remote from the penetrometer tip the integral may be decoupled to evaluate $2\tan^2\theta\int_0^{l_D}\chi_D d\chi_D=\tan^2\theta l_D^2=1$ and the steady pressure distribution around a conical penetrometer under constant velocity penetration of U is defined as (Elsworth 1991, 1998)

$$P_D=\frac{1}{R_D}e^{-U_D(R_D-x_D)} \tag{30}$$

where the nondimensional penetration velocity is $U_D=Ua/2c$. Behind the blunt tip of the penetrometer, and on the shaft, this reduces to $P_D=1/x_D$, allowing direct comparison with peak pressure magnitudes for the decelerating penetrometer. Most conveniently, this is plotted as $\log x_D$ versus $\log P_D$, where Eq. (30) plots as a straight line, as apparent in Fig. 4. In the zone ahead of the shoulder of the penetrometer ($0<x_D<l_D$), the pore fluid pressure magnitudes are singular in this range, due to the assumed zero radius of the conical tip of the cone. This steady behavior reduces to $P_D=1/x_D$ for large x_D, identical to the behavior for a blunt penetrometer. The $1/x_D$ distribution along the shaft is valid only at large separations from the tip, where the behavior for the tapered penetrometer approaches that for the blunt penetrometer for x_D greater than a few taper lengths, l_D. This is dependent only on the choice of taper angle for the cone, θ, as $\tan\theta=1/l_D$. For a decelerating penetrometer, the results asymptote to the distribution defined for $U_D\leqslant 10^{-1}$ for slow impact. Under these conditions the pore pressure distribution around the tip has not yet reached the dynamic steady state represented by the straight line for $P_D=1/x_D$. Physically, this represents the case where pressure transducers are far enough along the shaft that the penetrometer arrests before the transducer location may enter the induced pressure bulb. The pressure distribution for slow penetration will be near-spherical around the tip, and is influenced by the aggregate velocity along the path of the penetrometer, terminating at zero velocity.

Where the penetrometer impacts at a higher velocity, for example, for $U_D\geqslant 10^0$, the pressure distribution asymptotes to steady behavior. As nondimensional impact velocities become larger, the match to the steady behavior becomes closer, mainly because the embedment length increases proportionally to U_D as $x'_D=U_D/N_D$. These curves will be self-similar as the embedment length increases. Note that the pressure distributions are not truncated at the seabed, for $x_D>U_D/N_D$, because the medium is considered infinite, rather than semi-infinite, even though the effect of penetration is only applied following the presumed impact at the seabed at velocity U_0. As discussed previously, this effect will be small for typical embedment length.

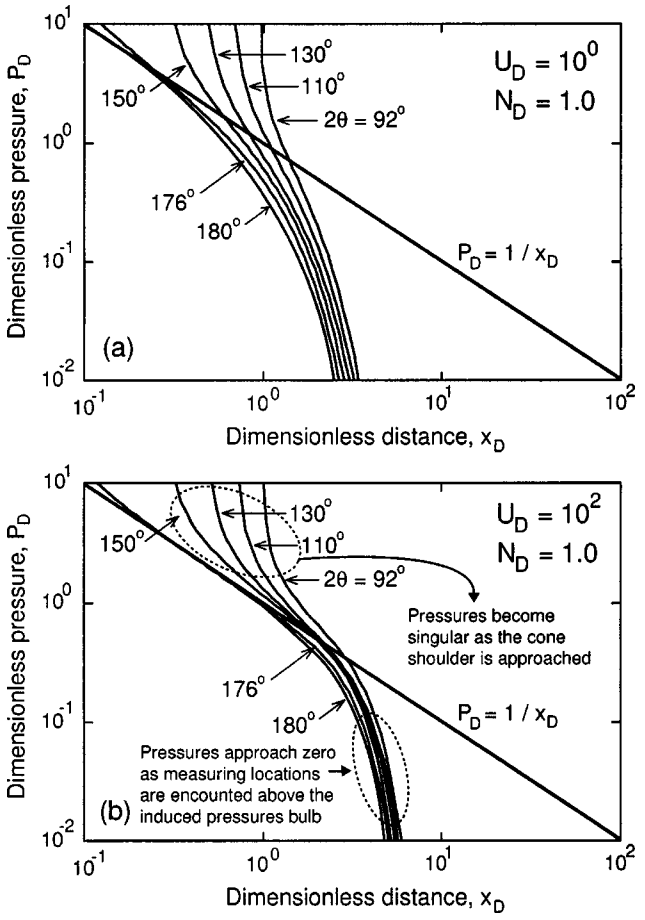

Fig. 4. Peak dimensionless pressure, P_D, measured along the penetrometer shaft illustrating the influence of penetrometer taper relative to the behavior for a blunt penetrometer, at the time of penetrometer arrest, $t'_D=\pi/N_D$. All pressures for both (a) and (b) correspond to dimensionless velocities of $U_D=10^0$ and $U_D=10^2$, and dimensionless strength of $N_D=1$.

The form of the contoured distribution of pressures around the tip is shown in Fig. 5 for a 120° cone ($2\theta=120°$) with the tip centered on the origin, using Eq. (29). The magnitude of P_D may also be determined in the zone ahead of the shoulder of the penetrometer ($0\leqslant x_D\leqslant l_D$), (Elsworth 1998). For high velocity impacts, the pressure distribution is cylindrical around the penetrometer, and markedly decreases in spread away from the penetrometer with an increase in nondimensional impact velocity, U_D. As the impact velocity is reduced, the pressure distribution becomes spherical, representing the dominant influence of the most recent portion of the advanced penetrometer, local to the tip. As nondimensional impact velocities are reduced below $U_D<10^{-1}$, the distributions become identical, indicating the control of pressure diffusion in dissipating the pressures, and a reduction in the relative influence of the migrating penetrometer. Importantly, the contoured representations are not truncated at the seabed surface, as the diffusive solution is for an infinite medium, even though the penetrometer was only ''turned-on'' as it impacted the seabed surface.

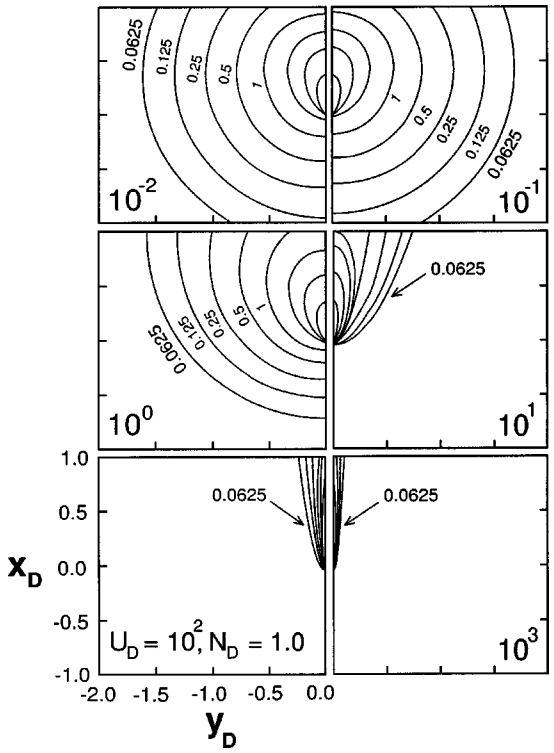

Fig. 5. Peak pressure distribution centered on the tip of a 120° (2θ) cone at $(x_D, y_D)=(0,0)$. Taper length is defined by semiapical angle as $l_D=1/\tan\theta$. Results document magnitudes of P_D in multiples of 2^{-n} within a radius of $R'_D=1$ of the cone tip. All figures locate the tip at the time of arrest, at the origin of the plot.

Postarrest

Postarrest behavior may be evaluated by superposing a moving dislocation of negative strength, beginning at the time of arrest, $t|_{\dot{x}'=0}$, defined as t'_D, over the positive strength moving dislocation that is applied continuously from the time of impact. Physically, the coincident moving dislocations of opposite strength, that initiate over the ''phantom'' trajectory of penetrometer, postarrest, enforce approximate boundary conditions for the system. Behavior at any time, $t_D > t'_D$, may be determined from the coincident and colinear moving dislocations, the first representing dilation from $0 \rightarrow t_D$ and the second representing an equivalent but opposite contractile volumetric dislocation from $t'_D \rightarrow t_D$ beginning from the location of the arrested tip at time t'_D. The effects of the coincident dislocation, ahead of the arrested tip, exactly cancel. The system equations follow directly from Eq. (29) as

$$P_D = \frac{2\tan^2\theta}{\sqrt{\pi}} \int_0^{l_D} \int_0^{t_D} \chi_D \frac{e^{-\tilde{R}_D^2/(t_D-\tau_D)}}{(t_D-\tau_D)^{3/2}} \times \cos\left[\frac{1}{2}N_D(t_D-\tau_D)\right] d\tau_D d\chi_D - \frac{2\tan^2\theta}{\sqrt{\pi}} \int_0^{l_D} \int_{t'_D}^{t_D} \chi_D \frac{e^{-\tilde{R}_D^2/(t_D-\tau_D)}}{(t_D-\tau_D)^{3/2}} \times \cos\left[\frac{1}{2}N_D(t_D-\tau_D)\right] d\tau_D d\chi_D \quad (31)$$

or alternatively as

$$P_D = \frac{2\tan^2\theta}{\sqrt{\pi}} \int_0^{l_D} \int_0^{t'_D} \chi_D \frac{e^{-\tilde{R}_D^2/(t_D-\tau_D)}}{(t_D-\tau_D)^{3/2}} \times \cos\left[\frac{1}{2}N_D(t_D-\tau_D)\right] d\tau_D d\chi_D \quad (32)$$

where the coordinate system migrates with the continuously migrating dislocation, postarrest, and pressures are referenced relative to this coordinate system. To transform to coordinates relative to the arrested penetrometer, a periodic transformation must be applied. Where the coordinate system $[\hat{x},\hat{y},\hat{z}]$ is chosen to represent locations relative to the arrested penetrometer ($[\hat{x}]$ is the distance of the pressure-measuring transducer behind the penetrometer tip), the linkage between the two coordinate systems is

$$x = \hat{x} - \frac{U_0}{b} + \frac{U_0}{b}\sin[b(t)]$$
$$y = \hat{y} \quad (33)$$
$$z = \hat{z}$$

where arrest always occurs at time, $t_{\text{arrest}} = t' = \pi/2b$ and

$$\tilde{x} = x - \frac{U_0}{b}\sin[b(t-\tau)] - \chi \quad (34)$$

The same nondimensional coordinate system may be invoked to yield the coordinate transform

$$x_D = \hat{x}_D - \frac{U_D}{N_D}\left[1 - \sin\left(\frac{1}{2}N_D t_D\right)\right] \quad (35)$$

or $\tilde{x}_D = \hat{x}_D + (U_D/N_D)[\sin(1/2N_D t_D) - 1] - (U_D/N_D)\sin[1/2N_D(t_D-\tau_D)] - \chi_D$ by substituting Eq. (35) into Eq. (34) and the result into $\tilde{R}_D = \sqrt{\tilde{x}_D^2 + y_D^2 + z_D^2}$. This results in an appropriate transform where the time to arrest is $t'_D = \pi/N_D$ and enables Eq. (31) to be directly evaluated.

Figure 6 describes the dissipation behavior following arrest at time t'_D. The time since arrest is defined as $(t_D - t'_D)$, and these plots, for transducer locations at 1/100 and 1/10 of the embedment length from the tip follow directly from the buildup data of Fig. 3. Maximum magnitudes of $P_D x_D$ track across from the buildup curves of Fig. 6, setting the peak pressure that falls following arrest. The dissipation behavior is included in Figs. 6(a–d) for a pressure transducer located one-hundredth $[x_D = (1/100)(U_D/N_D)]$ and one-tenth $[x_D = (1/10)(U_D/N_D)]$ of the embedment length back from the penetrometer tip. Similar to the pressure buildup behavior, dissipation is close to the behavior of a blunt penetrometer for large taper angles of the cone, θ, with different penetration rates, U_D, and material strengths, N_D. As in Figs. 6(b and c), dissipation is more rapid for a high nondimensional impact velocity, $U_D = 10^2$, and a transducer location further from the tip $[x_D = (1/10)(U_D/N_D)]$, and slowest for a low impact velocity, $U_D = 10^1$ with given transducer location $[x_D = (1/100)(U_D/N_D)]$, as in Fig. 6(a). The dissipation response is rapid for high nondimensional material strength, $N_D = 10^3$, with given high nondimensional impact velocity, $U_D = 10^4$, apparent in Fig. 6(d). As the cone taper approaches a blunt tip, as in Figs. 6(a–d), the pore pressures have a greater opportunity to build to the steady magnitude of $P_D x_D = 1$.

At low magnitudes of nondimensional penetration velocity, $U_D < 10^0$, the dissipation curves are all of similar form. At high impact velocities, $U_D \geq 10^1$, the dissipation response is rapid and results from the thin pressure ''skin'' that develops around the penetrometer shaft (Fig. 5). These results enable the time to 50%

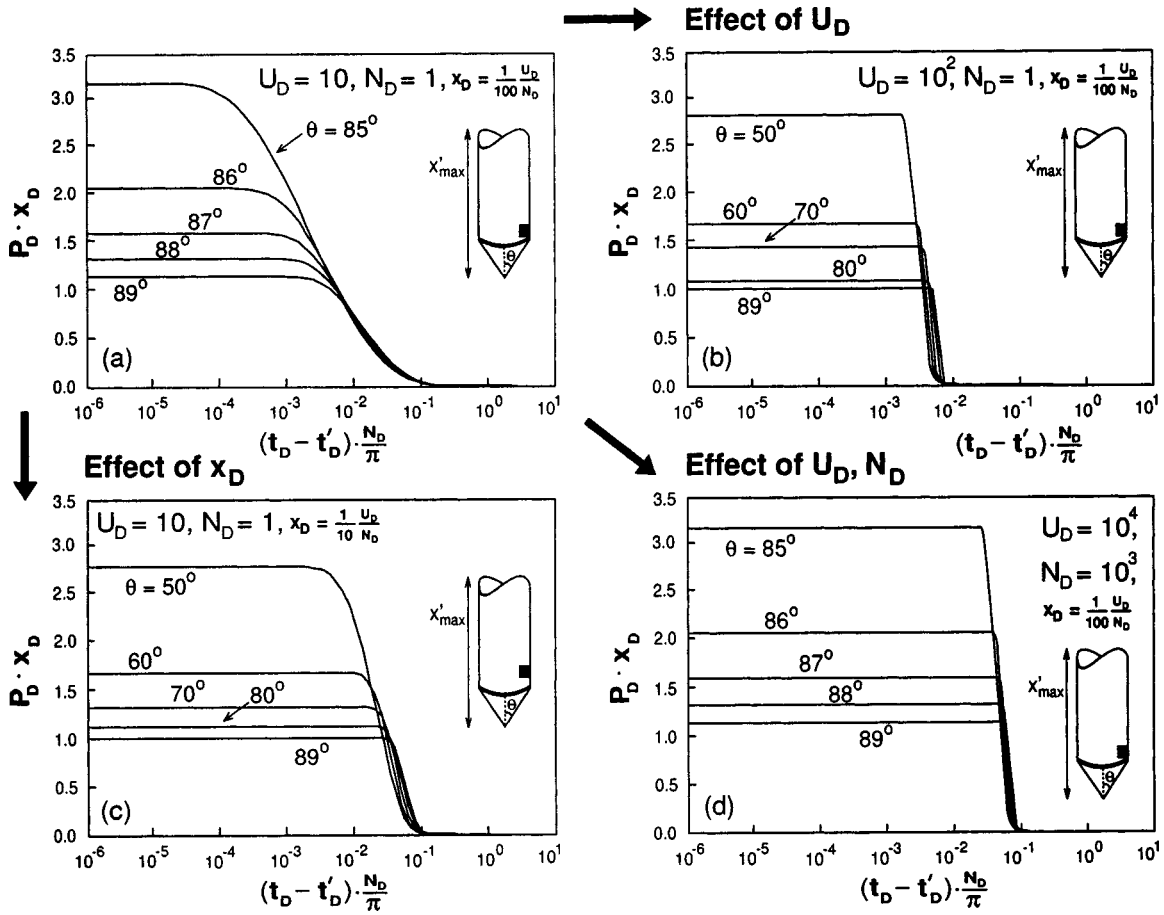

Fig. 6. Dissipation response following penetrometer arrest at time, t'_D. Change in nondimensional pressure is recorded as the product $P_D x_D$ for a transducer located a distance (a), (b), and (d) $x_D=(1/100)(U_D/N_D)$, (c) $x_D=(1/10)(U_D/N_D)$, behind the penetrometer tip. This represents a constant proportion of 1/100 and 1/10 of the total embedment length back from the tip. Pressure response is for various taper angles for the cone, θ, impact velocities, U_D, and material strengths, N_D.

pressure dissipation, t_{50}, to be determined, enabling hydraulic diffusivity, or consolidation coefficient, c, to be determined from the dissipation response.

Conclusions

A general treatment has been developed to represent the buildup and dissipation of pore pressures that result around a decelerating tapered penetrometer as it embeds within a poroelastic seabed. Pressure buildup and dissipation results have been specifically generated for various taper angles for the cone, θ, penetration rates, U_D, material strengths, N_D, and for two different monitoring locations $[x_D=(1/100)(U_D/N_D);(1/10)(U_D/N_D)]$. These strength magnitudes were selected as representative of a range of seabed sediment strengths. These results may be generalized for various strengths, by selecting appropriate groupings of nondimensional parameters. These parameter groups are different for buildup and for dissipation.

The assumed zero radius of the penetrometer in the zone of tip taper results in singular magnitudes of induced pore pressure in this region $(0\leqslant x_D\leqslant l_D; y_D=z_D=0)$. Behind the penetrometer tip, pore pressures asymptote to the blunt penetrometer distribution of $P_D=1/x_D$ as x_D becomes large. If the time of arrest and taper angle for the cone are known, the peak pressure magnitude, corresponding to that time may be defined. In the limit, and for small penetration velocities, $P_D x_D=1$, and confirms the $P_D=1/x_D$ pressure distribution along the shaft, apparent for steady penetration, as in Eq. (30).

The peak pressure for a tapered penetrometer may vary from this steady distribution due to both the effect of tip-taper and the unsteady behavior occasioned by penetrometer arrest. Tip-pressures are accentuated by the role of the tapered tip, as a result of pushing the singular pressures present at the tip shoulder further along the shaft. Further behind the tip, pressures measured beyond the penetration induced pressure bulb are lower than steady pressures, due to the brief period pressures are induced around the decelerating penetrometer.

Finally, since the nondimensional pressure, P_D, includes the magnitude of permeability, k, the peak generated pressure may be used to evaluate transport parameters of both permeability and consolidation coefficient or synonymous hydraulic diffusivity. From the definition of dimensionless pressure, P_D, of Eq. (24), permeability may be determined for peak insertion pressure, $p-p_s$, as

$$\frac{k}{\mu}=\frac{U_0 a}{4(p-p_s)x_D} \tag{36}$$

provided behavior has asymptoted to $P_D x_D=1$. The appropriateness of using $P_D x_D=1$ as a method of evaluating permeability may be determined only from dissipation data, used to evaluate U_D and from the form of the tip-local pressure distribution de-

fined in Fig. 4. In general, the relation of Eq. (36) cannot be used without correction. This is an important finding of this study.

Applying Eq. (36) to pore pressure data from pop-up pore pressure instrument (PUPPI) deployments (Urgeles et al. 2000) off La Palma, in the Canary Islands, enables permeabilities, k, and coefficient of consolidation, c, to be calculated directly from the peak pressure data and the dissipation response, respectively. For a 9.4° angle of cone taper, θ, an impact velocity, U_0, of 0.4 ms^{-1}, a penetrometer radius, a, of 0.019 m, a location of the pressure port (x) at 1.7 m behind the tip, and peak pressure ($p - p_s$) in the range 0.4–80 kPa, permeabilities may be recovered in the range 2×10^{-13} to 2×10^{-11} m^2. The evaluated results are higher than permeabilities obtained either from the tidal response, 10^{-18} to 10^{-16} m^2 (Urgeles et al. 2000) or from laboratory tests, 10^{-16} to 10^{-15} m^2 (Robert and Cramp 1996). This mismatch may result from rapid pressure dissipation along the shaft–soil interface, resulting in poor measurement of the peak pressure.

The solutions provide feasible mechanisms to evaluate transport properties of the penetrated seabed sediments. The first method involves the use of peak penetration-induced pressure as a proxy for permeability, that is independent of both drained compressibility measurements on recovered cores, or correlations with tidally forced pore-fluid pressures. The second method relates the matching of measured dissipation response to consolidation coefficient magnitudes, c, to be determined. These are determined by matching actual time-pressure responses with those for dimensionless-time and dimensionless-pressure to relate time directly with diffusive time, t_D, and thereby evaluate consolidation coefficient, c.

This full suite of penetration induced pore fluid pressure and subsequent dissipation responses offer the potential to better understand tip-local processes and the determination of sediment transport parameters from recorded pore pressure response.

Notation

The following symbols are used in this paper:

a = penetrometer of radius [L];
c = coefficient of consolidation [$L^2 T^{-1}$];
K = hydraulic conductivity [$L T^{-1}$];
k = absolute permeability [L^2];
N_c = dimensionless bearing capacity factor [—];
N_D = dimensionless strength [—];
P_D = dimensionless pressure [—];
p = absolute pore fluid pressure [$F L^{-2}$];
$p-p_s$ = excess pore pressure [$F L^{-2}$];
p_s = initial static fluid pressure [$F L^{-2}$];
q_u = bearing capacity [$F L^{-2}$];
R = radius of interest $R^2=x^2+y^2+z^2$ [L];
S_u = undrained cohesive strength [$F L^{-2}$];
t = time (current) [T];
t_D = dimensionless time (current) [—];
t_D' = dimensionless time of penetrometer arrest [—];
U = penetration rate [$L T^{-1}$];
U_D = dimensionless penetration rate [—];
U_0 = terminal velocity [$L T^{-1}$];
x = location of excess pore pressure [L];
x' = distance below seabed surface [L];
x,y,z = global Cartesian coordinates [—];
x_D,y_D,z_D = dimensionless Cartesian coordinates $(x/a;y/a;z/a)$ [—];
η = integration coefficient [—];
θ = semiapical angle [—];
μ = fluid dynamic viscosity [F T];
ξ = dimensionless inverse root time $\xi=R/\sqrt{c(t-\tau)}$ [—];
τ = time integrating parameter [—]; and
χ = global coordinate [—].

References

Acar, Y., and Tumay, M. T. (1986). "Strain field around cones in steady penetration." *J. Geotech. Eng.*, 112(2), 207–213.

Baligh, M. M. (1985). "Strain path method." *J. Geotech. Eng.*, 111(9), 1108–1136.

Baligh, M. M., and Levadoux, J. N. (1986). "Consolidation after undrained piezocone penetration. II: Interpretation." *J. Geotech. Eng.*, 112(7), 727–745.

Baligh, M. M., and Scott, R. F. (1976). "Analysis of deep wedge penetration in clay." *Geotechnique*, 26(1), 185–208.

Biot, M. A., and Willis, D. G. (1957). "The elastic coefficients of the theory of consolidation." *J. Appl. Mech.*, 24, 594–601.

Cleary, M. P. (1977). "Fundamental solutions for a fluid saturated porous solid." *Int. J. Solids Struct.*, 13(9), 785–806.

Davis, E. E., Horel, G. C., MacDonald, R. D., Villinger, H., Bennett, R. H., and Li, H. (1991). "Pore pres-sures and permeabilities measured in marine sediments with a tethered probe." *J. Geophys. Res. B*, 96(B4), 5975–5984.

Drescher, A., and Kang, M. (1987). "Kinematic approach to limit load for steady penetration in rigid-plastic soils." *Geotechnique*, 37(3), 233–246.

Elsworth, D. (1991). "Dislocation analysis of penetration in saturated porous media." *J. Eng. Mech.*, 117(2), 391–408.

Elsworth, D. (1992). "Pore pressure response due to penetration through layered media." *Int. J. Numer. Analyt. Meth. Geomech.*, 16(1), 45–64.

Elsworth, D. (1993). "Analysis of piezocone data using dislocation based methods." *J. Geotech. Eng.*, 119(10), 1601–1623.

Elsworth, D. (1998). "Indentation of a sharp penetrometer in a poroelastic medium." *Int. J. Solids Struct.*, 35(34–35), 4895–4904.

Fang, W. W., Langseth, M. G., and Schultheiss, P. J. (1993). "Analysis and application of in situ pore pressure measurements in marine sediments." *J. Geophys. Res. B*, 98(B5), 7921–7938.

Harvey, F., Rudolph, D. L., and Frape, S. K. (1997). "Measurement of hydraulic properties in deep lake sediments using a tethered pore pressure probe: Applications in the Hamilton Harbour, western Lake Ontario." *Water Resour. Res.*, 33(8), 1917–1928.

Ladanyi, B. (1963). "Expansion of a cavity in a saturated clay medium." *J. Soil Mech. Found. Div., Am. Soc. Civ. Eng.*, 89(4), 127–161.

Lee, D. R. (1977). "A device for measuring seepage flux in lakes and estuaries." *Limnol. Oceanogr.*, 22(1), 140–147.

Levadoux, J. N., and Baligh, M. M. (1986). "Consolidation after undrained piezocone penetration. I: Prediction." *J. Geotech. Eng.*, 112(7), 707–726.

Richards, A. F., Oien, K., Keller, G. H., and Lai, J. Y. (1975). "Differential piezometer probe for an in situ measurement of sea-floor porepressure." *Geotechnique*, 25(2), 229–238.

Robert, J., and Cramp, A. (1996). "Sediment stability on the western flanks of the Canary Islands." *Mar. Geol.*, 134, 13–30.

Robertson, P., Campanella, R., Gillespie, D., and Greig, J. (1986). "Use of piezometer cone data. In Proceedings of In Situ '86." *American Society of Civil Engineers Speciality Conf. GSP 6*, New York, 1263–1280.

Robertson, P., Sully, J., Woeller, D., Lunne, T., Powell, J. M., and Gillespie, D. (1992). "Estimating coefficient of consolidation from piezocone tests." *Can. Geotech. J.*, 29(4), 539–550.

Schultheiss, P. J., and Noel, M. (1986). ''Direct indication of pore water advection from pore pressure measurements in the Madeira Abyssal Plain sediments.'' *Nature (London)*, 320, 348–350.
Skempton, A. W. (1954). ''The pore pressure coefficients A and B.'' *Geotechnique*, 4(4), 143–147.
Skempton, A. W. (1959). ''Cast-in situ bored piles in London clay.'' *Geotechnique*, 9, 158.
Torstensson, B. A. (1977). ''The pore pressure probe.'' *Nord. Geotekniske Mote.*, 34, 34.1–34.15.
Tumay, M. T., Acar, Y. B., Cekirge, M. H., and Ramesh, N. (1985). ''Flow field around cone in steady penetration.'' *J. Geotech. Eng.*, 111(2), 193–204.
Urgeles, R., Canals, M., Roberts, J., and the SNV ''Las Palmas'' Shipboard Party. (2000). ''Fluid flow from pore pressure measurements off La Palma, Canary Islands.'' *J. Volcanol. Geotherm. Res.*, 101, 253–271.
Vesic, A. (1972). ''Expansion of cavities in infinite soil mass.'' *J. Soil Mech. Found. Div., Am. Soc. Civ. Eng.*, 98(3), 265–290.
Wang, K., and Davis, E. E. (1996). ''Theory for the propagation of tidally induced pore pressure variations in layered subseafloor formations.'' *J. Geophys. Res. B*, 101(B5), 11483–11495.
Watts, A. B., and Masson, D. G. (1995). ''A giant landslide on the north flank of Tenerife Canary Islands.'' *J. Geophys. Res. B*, 100(B4), 24487–24498.